## PAPER

Check for updates

# Copper-doped lanthanum manganite La$_{0.65}$Ce$_{0.05}$Sr$_{0.3}$Mn$_{1-x}$Cu$_x$O$_3$ influence on structural, magnetic and magnetocaloric effects

M. Chebaane,[a] R. Bellouz, [iD] *[a] Ma. Oumezzine,*[a] E. K. Hlil[b] and A. Fouzri[a]

Bulk nanocrystalline samples of La$_{0.65}$Ce$_{0.05}$Sr$_{0.3}$Mn$_{1-x}$Cu$_x$O$_3$ ($0 \leq x \leq 0.15$) manganites are prepared by the sol–gel based Pechini method. The effect of the substitution for Mn with Cu upon the structural and magnetic properties has been investigated by means of X-ray diffraction (XRD), Raman spectroscopy and dc magnetization measurements. The structural parameters obtained using Rietveld refinement of XRD data showed perovskite structures with rhombohedral ($R\bar{3}c$) symmetry without any detectable impurity phase. Raman spectra at room temperature reveal a gradual change in phonon modes with increasing copper concentration. The analysis of the crystallographic data suggested a strong correlation between structure and magnetism, for instance a relationship between a distortion of the MnO$_6$ octahedron and the reduction in the Curie temperature, $T_c$. A paramagnetic to ferromagnetic phase transition at $T_C$ is observed. The experimental results confirm that Mn-site substitution with Cu destroys the Mn$^{3+}$–O$^{2-}$–Mn$^{4+}$ bridges and weakens the double exchange (DE) interaction between Mn$^{3+}$ and Mn$^{4+}$ ions, which shows an obvious suppression of the FM interaction in the La$_{0.65}$Ce$_{0.05}$Sr$_{0.3}$Mn$_{1-x}$Cu$_x$O$_3$ matrix. The maximum magnetic entropy change $-\Delta S_M^{max}$ is found to decrease with increasing Cu content from 4.43 J kg$^{-1}$ K$^{-1}$ for $x = 0$ to 3.03 J kg$^{-1}$ K$^{-1}$ for $x = 0.15$ upon a 5 T applied field change.

## 1. Introduction

Recently, perovskite manganites of R$_{1-x}$A$_x$MnO$_3$ (where R and A are trivalent rare earth and divalent alkaline earth ions, respectively) have been the subject of intense research due to their interesting physical properties around the ferromagnetic (FM)–paramagnetic (PM) transition temperature (the Curie temperature, $T_C$), such as the colossal magnetoresistance (CMR), the magnetocaloric effects (MCE) (related to a large magnetic entropy change) and the strong correlation between structural and magnetic properties. Doped lanthanum based manganites have been used in many technological applications, including magnetic recording, high-density data storage, hard disks, magnetic sensors, spin-electronic devices, and magnetic refrigerants.[1–4]

These materials offer a high degree of chemical flexibility leading to complex interplay between structural, electrical and magnetic properties. The double exchange (DE) effect in which e$_g$ electrons transfer between adjacent Mn$^{3+}$ and Mn$^{4+}$ ions and the Jahn–Teller effect were used to understand FM–PM transition and CMR in manganites.[5,6] A prominent feature of most

manganites is that they will undergo a ferromagnetic–paramagnetic (FM–PM) phase transition at the Curie temperature $T_C$ associated with an metal–insulator (M–I) transition at temperature $T_{MI}$, which explains the fact that there exists a close relationship between the electrical and magnetic properties of manganites.[7,8] Average ionic radius, electronic configuration, valance state and the concentration of the doping element are important parameters for tuning the magnetic and electronic properties of these materials.[9]

On the other hand, the synthesis technique greatly influences the physical and chemical characteristics of the rare-earth perovskite materials. There are various methods to synthesize the manganites compounds among them the Pechini sol–gel method. This method has been used successfully to produce high-quality specimens due to these potential advantages such as better homogeneities, lower processing temperatures, short annealing times, high purity of materials and improved material properties.

In manganites, it is possible to dope at both R-site and Mn-site, much research has been done on the substitution at the R-site with transition elements[10–12] and/or rare-earths Eu,[13] Ce,[14] Pr,[15] which can modify the Mn$^{3+}$–O$^{2-}$–Mn$^{4+}$ network and in turn will intensively affect the intrinsic physical properties, such as ferromagnetism and (MCE). The substitution at the Mn site in perovskite oxides, with other transition metal ions,[16–20] is more important because it not only modifies the Mn$^{3+}$–O$^{2-}$–Mn$^{4+}$ network but also brings about many new exchange interactions between the Mn ion and the doped transition metal ions.

*[a] Laboratory of Physical Chemistry of Materials, Faculty of Sciences of Monastir, University of Monastir, 5019 Monastir, Tunisia. E-mail: bellouzridha@yahoo.fr; Oumezzine@hotmail.co.uk*

*[b] Institut Néel, CNRS–Université J. Fourier, B.P. 166, 38042 Grenoble, France*

Amongst the doping at Mn sites with transition elements, Cu substitution has been particularly investigated because of the special nature of its variable valence.[21-31] In particular, Kim et al.[30,31] reported the coexistence of $Cu^{2+}$ and $Cu^{3+}$ ions with $Cu^{2+}$ dominant was found in their samples, and was thought to be responsible for the variations of the lattice parameters, Mn/Cu–O bond length and Mn/Cu–O–Mn/Cu bond angle. The doping of Cu changes the $Cu^{2+}/Cu^{3+}$ ratio and therefore the $Mn^{3+}/Mn^{4+}$ ratio, which may affect the electron carrier density, causing an intrinsic effect on the $Mn^{3+}–O^{2-}–Mn^{4+}$ DE network.

The objective of this work was to synthesize nanocrystalline samples of $La_{0.65}Ce_{0.05}Sr_{0.3}Mn_{1-x}Cu_xO_3$ with an extended doping levels up to $x = 0.15$ and study the influence of copper-doping at Mn-site on the structural, magnetic and magneto-caloric properties.

## 2. Experimental procedure

### 2.1. Synthesis

Nanocrystalline samples of $La_{0.65}Ce_{0.05}Sr_{0.3}Mn_{1-x}Cu_xO_3$ ($0 \leq x \leq 0.15$) were prepared using the Pechini sol–gel method and a mixture of oxides and precursors, $La(NO_3)_3 \cdot 6H_2O$, $Sr(NO_3)_2$, $Ce(NO_3)_3 \cdot 6H_2O$, $Mn_2O_3$ and $Cu(NO_3)_2 \cdot 3H_2O$. The stoichiometric amounts of precursors were dissolved in distilled water at 90 °C and then a suitable amount of citric acid and ethylene glycol as coordinate agents were added. The resulting gel was pre-calcined (673 K for 3 h) to eliminate the organic material, ground and calcined again (973 K for 15 h) to eliminate the residual organic material. The obtained powder was then pressed into pellets (13 mm in diameter and 2–3 mm thick under a pressure of 5 ton $cm^{-2}$). After that, the powder was sintered at 1173 K for 12 h in air.

### 2.2. Characterization

The morphological properties of the samples were investigated by scanning electron microscopy (SEM) on a JSM-6400 apparatus working at 20 kV. The structure and phase purity were checked by powder X-ray diffraction (XRD) using a "Panalytical X pert Pro" diffractometer with Cu $K_\alpha$ radiation ($k = 1.5406$ Å). Data for Rietveld refinement were collected in the range of 2 h from 10° to 120° with a step size of 0.017° and a counting time of 18 s per step. Raman scattering data was collected in the frequency range 100–1000 $cm^{-1}$ using a Raman spectrometer. Magnetic measurements versus temperature and magnetic applied field were realized using a SQUID (Quantum Design) developed at Louis Neel Laboratory of Grenoble. The isothermals $M$ versus $H$ at various temperatures around $T_C$ have been measured in applied fields up to 5 T.

## 3. Results and discussion

### 3.1. Structural properties

Fig. 1(a) shows the experimental XRD plots for the samples $La_{0.65}Ce_{0.05}Sr_{0.3}Mn_{1-x}Cu_xO_3$ with $x = 0$, 0.05, 0.1 and 0.15. We first discuss the structural parameters of the studied samples in present work. Using the Rietveld refinement method, we noted that all samples are single-phase with a rhombohedral structure of the $R\bar{3}c$ space group (no. 167), in which the (La, Ce, Sr) atoms are at 6a (0, 0, 1/4) positions, (Mn, Cu) at 6b (0, 0, 0) and O at 18e ($x$, 0, 1/4). These results are consistent with the values of the Goldschmidt tolerance factor $t_G$:
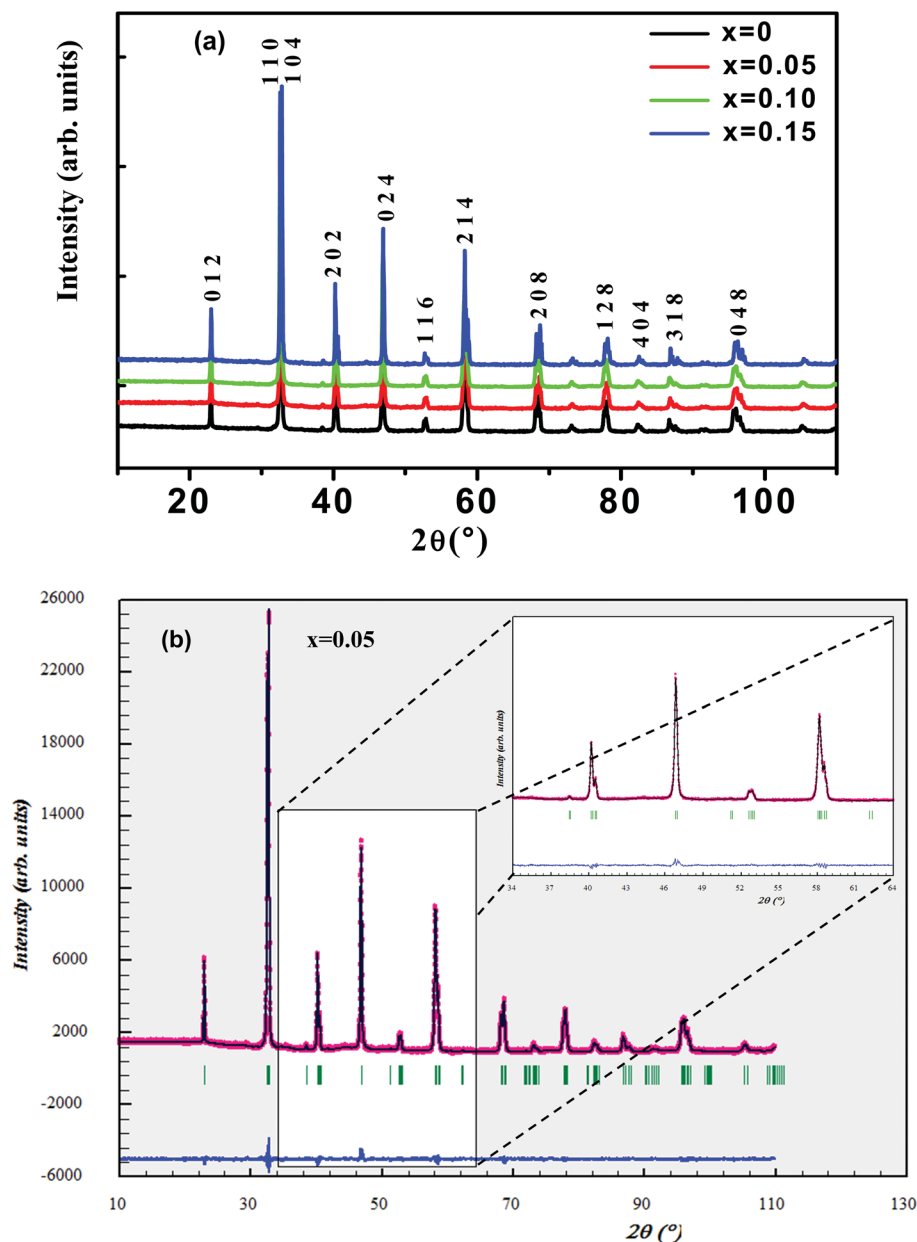
$$t = \frac{\langle r_A \rangle + r_O}{\sqrt{2}(\langle r_B \rangle + r_O)} \tag{1}$$

where $r_A$, $r_B$ and $r_O$ are respectively the average ionic radii of A and B perovskite sites and of the oxygen anions. The tolerance factor is an important structural parameter, which reflects the local microscopic distortion from the ideal perovskite ($ABO_3$) structure ($t = 1$), for which the B–O–B bond angle $\theta$ is equal to 180°. The values of $t_G$ were estimated and listed in Table 1.

The structural parameters were refined by the standard Rietveld refinement method using the FullProf program.[32] We utilize the pseudo-Voigt function in order to fit parameters to the experimental data set. The parameters used are: a scale factor, a zero shifting factor, three cell parameters, five shapes and width of the peak factors, one global thermal factor and two asymmetric factors, the background was refined by a linear interpolation between a set background points with refinable heights. The weighted profile factor $R_{wp}$, the goodness of fit $\chi^2$, and the difference between the calculated and observed profiles were evaluated at each refinement cycle to determine the refinement quality. The final refinement analysis shows that the experimental spectra and the calculated values obtained by the Rietveld refinement are in good agreement with each other, and all observed peaks have been suitably indexed. The calculated results are shown in Fig. 1(b) and Table 1. One can see from Table 1 that both the lattice parameters ($a = b$, and $c$) and unit cell volume show a monotonous decrease with increasing Cu content. Similar structural variation with Cu doping at Mn sites was reported in ref. 24, 26, 29 and 30. (XPS) studies of Cu-doped manganites have shown that Cu ions exist in mixed-valence states: $Cu^{2+}$ and $Cu^{3+}$ with dominant $Cu^{2+}$.[30,31] The crystal structure and lattice parameters were affected because of the mismatch of ionic radius between the dopant and Mn ions. The B-site ionic radius of $Cu^{2+}$ (0.73 Å) is larger than $Mn^{3+}$ ($Mn^{4+}$) and the ionic radius of $Cu^{3+}$ (0.54 Å) is close to that of $Mn^{4+}$ (0.53 Å) and smaller than the radius of the high spin state of $Mn^{3+}$ (0.645 Å).[33] Further, it is expected that $Cu^{2+}$ ions substitute $Mn^{3+}$ ions and $Cu^{3+}$ ions substitute $Mn^{4+}$ ions. Furthermore, substitution of $Cu^{2+}$ for $Mn^{3+}$ and $Cu^{3+}$ for $Mn^{4+}$ would lead to a proportionate conversion of $Mn^{3+}$ to $Mn^{4+}$ and $Mn^{4+}$ to $Mn^{3+}$. But the ionic state of $Cu^{2+}$ is expected to be dominant in the samples, therefore, the overall copper doping effect leads to a change in the relative fraction of different valence Mn ions, which results an increase in the number of $Mn^{4+}$ ions in order to preserve charge neutrality and therefore the unit cell volume is found to decrease.

Fig. 2(a and b) shows crystal structure of $La_{0.65}Ce_{0.05}Sr_{0.3}Mn_{1-x}Cu_xO_3$ showing $MnO_6$ octahedron generated with the help of program VESTA (Visualization for Electronic and Structural Analysis) using refined cell parameters, space group and positional parameters of atoms.[34] It is represented from the

**Fig. 1** (a) XRD patterns of $La_{0.65}Ce_{0.05}Sr_{0.3}Mn_{1-x}Cu_xO_3$ ($0 \leq x \leq 0.15$) compounds at room temperature. (b) Rietveld refinement profile for $x =$ 0.05 performed using FULLPROF. Open circles correspond to experimental data and the lines are fits. Vertical bars represent the Bragg reflections for the space group $R\bar{3}c$. The difference pattern between the observed data and fits is shown at the bottom. The inset shows a zoom in the region between $2\theta$: 34–64°.

figure that (La/Ce/Sr) cations occupies A-site in $ABO_3$ type perovskite structure and are surrounded by 12 oxygen ions while Mn ion occupies the octahedral position (B site) surrounded by six oxygen ions, thus, forming a $MnO_6$ octahedron Fig. 2(a).

The surface morphology of samples examined by scanning electron microscopy (SEM) is illustrated in Fig. 2(c). The SEM images show that the particles have an almost homogeneous distribution. The average crystallite size of the samples are obtained by applying the following Rietveld refinement formula $CS = \dfrac{180\lambda}{\pi\sqrt{IG}}$, where $k$ is the X-ray wavelength and IG is the

Gaussian size parameter given by Rietveld refinement. In all samples a nanometric size for the crystallites is found, between 77 nm and 94 nm ($\pm 2$ nm), which is related to the moderate synthesis temperatures of these samples, obtained from very reactive precursors from sol–gel procedures. These values are close to those shown by SEM micrographs (the average particles size is $\sim$100 ($\pm$10 nm).

### 3.2. Raman spectroscopy

Raman spectroscopy is a powerful and sensitive tool for the non-destructive investigation and characterization of all kinds

**Table 1** Detailed results of Rietveld refinement of $La_{0.65}Ce_{0.05}Sr_{0.3}$-$Mn_{1-x}Cu_xO_3$ ($0 \leq x \leq 0.15$) samples at room temperature

| $x$ | 0 | 0.05 | 0.10 | 0.15 |
|---|---|---|---|---|
| Space group | $R\bar{3}c$ | $R\bar{3}c$ | $R\bar{3}c$ | $R\bar{3}c$ |
| Lattice parameters | | | | |
| $a = b$ (Å) | 5.5037 (1) | 5.4995 (2) | 5.4979 (2) | 5.4954 (1) |
| $c$ (Å) | 13.3691 (2) | 13.3549 (3) | 13.3452(1) | 13.3332 (3) |
| $V$ (Å$^3$) | 350.70 (2) | 349.79 (2) | 349.29 (2) | 348.71 (1) |
| (La, Ce, Sr) $B_{iso}$ (Å$^2$) | 0.78 (3) | 0.64 (3) | 0.62 (3) | 0.35 (4) |
| (Mn, Cu) $B_{iso}$ (Å$^2$) | 0.29 (4) | 0.18 (2) | 0.14 (4) | 0.13 (7) |
| (O) $B_{iso}$ (Å$^2$) | 0.8 (1) | 0.65 (1) | 0.61 (1) | 0.32(1) |
| (O) $x$ | 0.462 (1) | 0.462 (4) | 0.461 (2) | 0.459 (1) |
| $d_{(Mn, Cu-O)}$ (Å) | 1.9518 (4) | 1.9522 (5) | 1.9533 (8) | 1.9539 (8) |
| $\theta_{(Mn, Cu-O-Mn, Cu)}$ (°) | 167.64 (2) | 167.53 (2) | 167.37 (3) | 167.11 (5) |
| $W$ ($\times 10^{-2}$) (u.a.) | 9.570 | 9.562 | 9.554 | 9.552 |
| $t_G$ | 0.976 | 0.979 | 0.981 | 0.984 |
| $T_G^{DRX}$ (nm) | 77 | 83 | 85 | 94 |
| $R_{wp}$ (%) | 3.68 | 3.34 | 3.32 | 3.61 |
| $R_p$ (%) | 2.90 | 2.61 | 2.60 | 3.36 |
| $R_F$ (%) | 1.71 | 1.55 | 1.49 | 2.39 |
| $\chi^2$ (%) | 1.71 | 1.54 | 1.53 | 2.79 |

of materials. This technique is useful in understanding crystal symmetry, the local structural distortion and its dependence on doping. Our manganites samples shows rhombohedral crystal symmetry using the $R\bar{3}c$ space group that assumes six equal distances of the Mn–O bonds of $MnO_6$ octahedra (Fig. 2(b)). This structure can be described with respect to the ideal cubic structure by considering a rotation of $MnO_6$ octahedra about the [111] pseudo cubic diagonal. According to the group theory, for $R\bar{3}c$ ($D_{3d}^6$) rhombohedral structure, thirty vibrational degrees of freedom at the $\Gamma$ point are distributed among the irreducible representation as:

$$\Gamma (D_{3d}^6) = 2A_{1u} + 3A_{2g} + A_{1g} + 4A_{2u} + 4E_g + 6E_u$$

The rhombohedral distortion gives rise to five Raman active modes.

Room temperature Raman spectrum of as synthesized $La_{0.65}Ce_{0.05}Sr_{0.3}Mn_{1-x}Cu_xO_3$ ($x = 0, 0.05, 0.10$ and $0.15$) samples in the frequency range of 200–900 cm$^{-1}$ is shown in Fig. 3(a). Five vibration modes have been identified, one ($A_{1g}$) and four ($E_g$). These broad bands are located at 162 ($A_{1g}$), 302 ($E_g$), 424 ($E_g$), 460 ($E_g$) and 667–703 ($E_g$) cm$^{-1}$, which are associated with



**Fig. 2** (a) Crystal structure of $La_{0.65}Ce_{0.05}Sr_{0.3}MnO_3$ (b) 3D view showing $MnO_6$ octahedron (c) SEM images of ($x = 0$ and $x = 0.15$) samples.

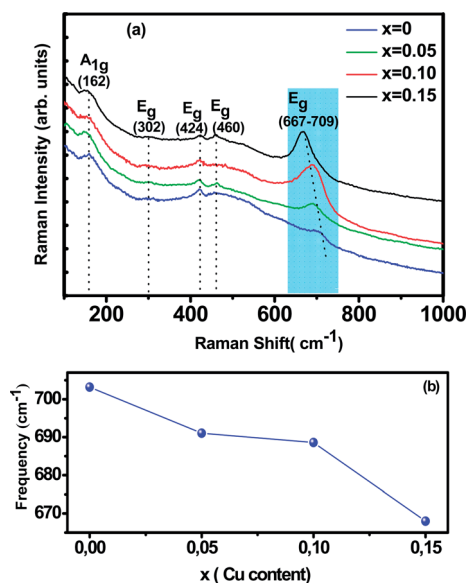Fig. 3 Raman spectrum of $La_{0.65}Ce_{0.05}Sr_{0.3}Mn_{1-x}Cu_xO_3$ ($x = 0$, 0.05, 0.10 and 0.15).

rotational-, bending-, and stretching-like vibrations of the $MnO_6$ octahedra, respectively.[35,36] It has been noticed from the graph that with increasing Cu concentration, the Raman scattering intensity of the phonon modes are increasing. The frequencies of the experimental peaks are plotted with doping level for the high-frequency mode $E_g$ in Fig. 3(b). This mode shows a substantial shift toward lower frequencies (a downshift of about 30 cm$^{-1}$) as a function of Cu concentration. These shifts are related to the change in the average (Mn/Cu)–O distance.[37] Similar observations have been reported for some other perovskite compounds with distorted rhombohedral lattice.[35,38,39]

In this work, we underline the $E_g$ mode allowed for the symmetric stretching vibration of oxygen in $MnO_6$ octahedra. It is reasonable to relate the changes on the $E_g$ mode frequency to the modifications of the oxygen octahedral $MnO_6$. Moreover, the introduction of substitutional defect in the B-site (like Cu) has a strong effect in the structural changes of the lattice. Since Cu substitution induces a strong local stress, it can be expected that $(Mn/Cu)O_6$ octahedra rotate, and the Mn–O bond lengths decrease under this compression.[40]

### 3.3. Magnetic properties

The magnetization of $La_{0.65}Ce_{0.05}Sr_{0.3}Mn_{1-x}Cu_xO_3$ ($0 \leq x \leq 0.15$) as a function of temperature from 5 K to 400 K under an applied field of 100 Oe is shown in Fig. 4(a).

All samples exhibit a clear transition from paramagnetic to ferromagnetic state with decreasing temperature. The Curie temperature $T_C$ is the temperature at which the absolute value of $dM/dT$ is maximum (inset Fig. 4(a)), are summarized in Table 2.

One can see that $T_C$ decreases monotonically with increasing Cu-doping content. This behavior is consistent with those reported previously on Mn-site substitution of copper.[22,26] However, the Mn site substitution of $Cu^{2+}/Cu^{3+}$ with localized



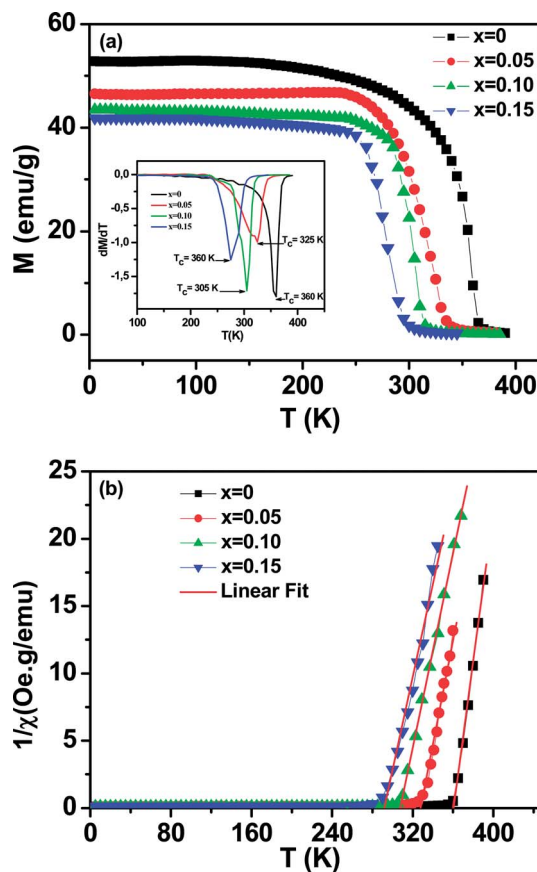Fig. 4 Temperature dependence of the magnetization for $La_{0.65}$-$Ce_{0.05}Sr_{0.3}Mn_{1-x}Cu_xO_3$ ($x = 0.10$ and $x = 0.15$) measured in field cooling (FC) mode at an applied magnetic field of $\mu_0H = 500$ Oe. Inset (a) the temperature derivative $dM/dT$. (b) Temperature dependence of the inverse of magnetic susceptibility $1 = \chi$. The red line presents the linear fit at high temperature.

electrons ($Cu^{2+}$: $t_{2g}^6 eg^3$, $Cu^{3+}$: $t_{2g}^6 eg^2$) reduces the amount of $Mn^{3+}$ ($t_{2g\uparrow}^3 eg_\uparrow^1$) with itinerate $eg_\uparrow^1$ electron and converts $Mn^{3+}$ ($t_{2g\uparrow}^3 e_{g\uparrow}^1$) to $Mn^{4+}$ ($t_{2g\uparrow}^3 eg_\uparrow^0$) for charge neutrality, directly affecting the DE interaction, weakening the ferromagnetic coupling between $Mn^{3+}$ and $Mn^{4+}$ ions and leads to the lower ordering of FM transition temperature and suppresses the FM interaction. On the other hand, the decrease in $T_C$ is also closely related to the decrease in the one-electron band-width $W$ of $e_g$ electron[35] (Table 1) due to the increase of $d_{Mn/Cu–O}$ bond length and the decrease of $\theta_{<Mn/Cu–O–Mn/Cu>}$ bond angle caused by copper doping. The reduction of the parameter $W$ is related to the weakening of the overlap between the O-2p and the Mn-3d orbital, which in turn decreases the (DE) interaction.

To get a clear knowledge about the magnetic interaction for the $La_{0.65}Ce_{0.05}Sr_{0.3}Mn_{1-x}Cu_xO_3$, the magnetic susceptibility ($\chi$) could be fitted to the Curie–Weiss law: $\chi = C/(T - \theta_p)$; where $\theta_p$ is the Curie–Weiss temperature (the temperature at which $\chi^{-1}$ intercepts the temperature axis) and $C$ is the Curie constant were determined by linear fitting of the temperature dependent $\chi^{-1}$ data in the high temperature paramagnetic region, as displayed in Fig. 4(b) and the values are given in Table 2.

**Table 2** Values of the Curie temperature $T_C$, the Curie constant $C$, the Curie–Weiss temperature $\theta_P$ and the experimental and theoretical effective paramagnetic moment ($\mu_{eff}^{exp}$) and ($\mu_{eff}^{th}$) for La$_{0.65}$Ce$_{0.05}$Sr$_{0.3}$Mn$_{1-x}$Cu$_x$O$_3$ ($0 \leq x \leq 0.15$)

|  | $T_C$ (K) | $\theta_P$ (K) | $C$ | $\mu_{eff}$ (exp) ($\mu_B$) | $\mu_{eff}$ (cal) ($\mu_B$)[a] | $\mu_{eff}$ (cal) ($\mu_B$)[b] |
|---|---|---|---|---|---|---|
| $x = 0$ | 360 | 353 | 2.777 | 4.71 | 4.61 | 4.61 |
| $x = 0.05$ | 330 | 323 | 2.607 | 4.56 | 4.45 | 4.52 |
| $x = 0.10$ | 305 | 300 | 2.769 | 4.70 | 4.27 | 4.43 |
| $x = 0.15$ | 275 | 270 | 2.894 | 4.81 | 4.09 | 4.34 |

[a] Under the assumption that all of the Cu ions exist in Cu$^{2+}$ state. [b] Under the assumption that all of the Cu ions exist in Cu$^{3+}$ state.

The positive sign of $\theta_P$ values implies the ferromagnetic nature of the magnetic interactions between spins and are basically consistent with the values of $T_C$.
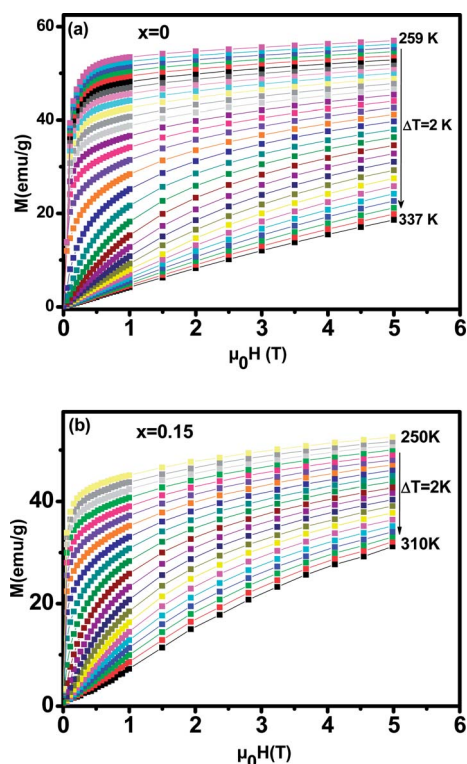
From the estimated Curie constant ($C$), we have deduced the experimental effective moment ($\mu_{eff}^{exp}$) using the following relation: $(\mu_{eff}^{exp})^2 = \dfrac{3k_B M_m C}{N_A \mu_B^2}$; where $N_A = 6.023 \times 10^{23}$ mol$^{-1}$ is the number of Avogadro, $\mu_B = 9.274 \times 10^{-21}$ emu is the Bohr magneton, $M_m$ is the molecular weight and $k_B = 1.38016 \times 10^{-16}$ erg K$^{-1}$ is the Boltzmann constant.

The theoretical effective paramagnetic moment ($\mu_{eff}^{th}$) was calculated using the calculated Mn$^{3+}$/Mn$^{4+}$ contents under the assumption that all the Cu ions exist in either Cu$^{2+}$ or Cu$^{3+}$ state. The spin-only magnetic moments for free Mn$^{3+}$, Mn$^{4+}$, Cu$^{2+}$ and Cu$^{3+}$ are 4.89$\mu_B$, 3.87$\mu_B$, 1.73$\mu_B$, 2.83$\mu_B$, respectively. The obtained values of ($\mu_{eff}^{exp}$) and ($\mu_{eff}^{th}$) are listed in Table 2. The experimental ($\mu_{eff}^{exp}$) value is little larger than the calculated value
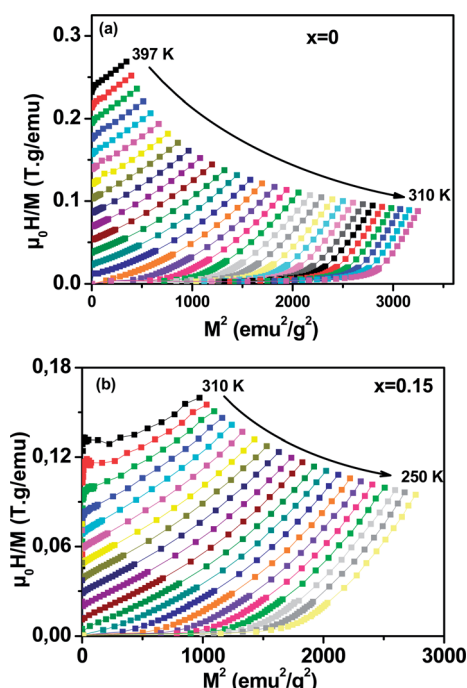
using the spin-only moment. Such a difference in ($\mu_{eff}$) value may be ascribed to the appearance of short-range FM interactions in the paramagnetic state. This result is commonly observed in manganites.[8,41,42]

In order to investigate the magnetic behavior at low temperatures, we have performed magnetization measurements as a function of the applied magnetic field $\mu_0 H$ up to 5 T at various temperatures. We plot in Fig. 5 the magnetization evolution *versus* the applied magnetic field obtained at different temperature (isothermal magnetization) for (a) $x = 0$, and (b) $x = 0.15$ samples. At a given lower fields, ($M$–$H$–$T$) curves show a rapid increase and get saturated at higher fields. For all the studied samples, the magnetization has been found to increase with decreasing temperature in the selected temperature range, where thermal fluctuation of spins decreases with decreasing temperature.

To determine the nature of the FM–PM phase transition (first or second order) for our samples, we plotted in Fig. 6(a and b) the Arrott plot[43] ($\mu_0 H/M$ *versus* $M^2$) for $x = 0$ and $x = 0.15$.



**Fig. 5** Isothermal magnetization *versus* magnetic field around $T_C$ of La$_{0.65}$Ce$_{0.05}$Sr$_{0.3}$Mn$_{1-x}$Cu$_x$O$_3$, (a) for $x = 0$ and (b) for $x = 0.15$.



**Fig. 6** Arrott plot of $\mu_0 H/M$ *vs.* $M^2$ at different temperatures for La$_{0.65}$Ce$_{0.05}$Sr$_{0.3}$Mn$_{1-x}$Cu$_x$O$_3$, (a) $x = 0$ and (b) $x = 0.15$.

According to the Banerjee criterion,[44] all of the $M^2$ vs. $\mu_0H/M$ curves show positive slopes without infection points, which is characteristic of second order transitions.

### 3.4. Magnetocaloric effect and second-order magnetic phase transition

MCE is an intrinsic property of magnetic materials. It is the response of the material toward the application or removal of a magnetic field. This response is maximized when the material is near its magnetic ordering temperature. In an isothermal process, the magnetic entropy change of the materials can be derived from the Maxwell relation as shown below:[45]

$$\Delta S_M = \mu_0 \int_0^H \left(\frac{\partial M(H,T)}{\partial T}\right)_H dH \qquad (2)$$

The magnetic entropy changes, $\Delta S_M$, of $La_{0.65}Ce_{0.05}Sr_{0.3}Mn_{1-x}Cu_xO_3$ ($x = 0$, 0.05, 0.1 and 0.15) have been calculated using the Maxwell relation[46] and are plotted in Fig. 7 as a function of temperature and field.

The maximum value of magnetic entropy change $\Delta S_M$ is found to be around $T_C$ and it increases with increasing the magnetic applied field due to the enhancement of FM interactions. As the Cu content increases the magnitude of $\Delta S_M$ decreases under a given field strength. Indeed, under the magnetic field change from 0 to 5 T, the values of $|\Delta S_M^{max}|$ observed for $x = 0.00$, 0.05, 0.1 and $x = 0.15$ are found to be 4.43,

5.15, 3.37 and 3.03 J kg$^{-1}$ K$^{-1}$, respectively. The value of $|\Delta S_M^{max}|$ for $\mu_0H = 1$ and 5 T are listed in Table 2 along with related compounds[47,48] for easy comparison.

Relative cooling power (RCP) is another important parameter to quantify the efficiency of the magnetocaloric material. It is a measure of how much heat can be transferred between the cold and the hot tanks in one ideal refrigeration cycle. It can be defined as

$$RCP = -\Delta S_M^{max} \times \delta_{FWHM}, \qquad (3)$$

where $\delta_{FWHM} = \Delta T$ is the full-width at half maximum peak and $-\Delta S_M^{max}$ is the maximum value of magnetic entropy change which is occurred at Curie temperature.

The RCP values of the $La_{0.65}Ce_{0.05}Sr_{0.3}Mn_{1-x}Cu_xO_3$ are evaluated under the magnetic field changes of 1 and 5 T. For a comparison $T_C$ and magnetocaloric parameters of some relevant manganites in the literature are listed in Table 3.

The maximum value of RCP is obtained for $x = 0.05$, which is 43% of that of pure Gd, the prototype magnetic refrigerant material (RCP = 410 J kg$^{-1}$).[48] Our results indicate that this compound is promising for room temperature magnetic refrigeration.

For further clarification of the phase transition of the samples as an alternative to the Banerjee criterion[44] we used the phenomenological universal curve method, proposed by Franco et al.,[49,50] which is a general approach to determine the order of the phase transition. In order to construct this
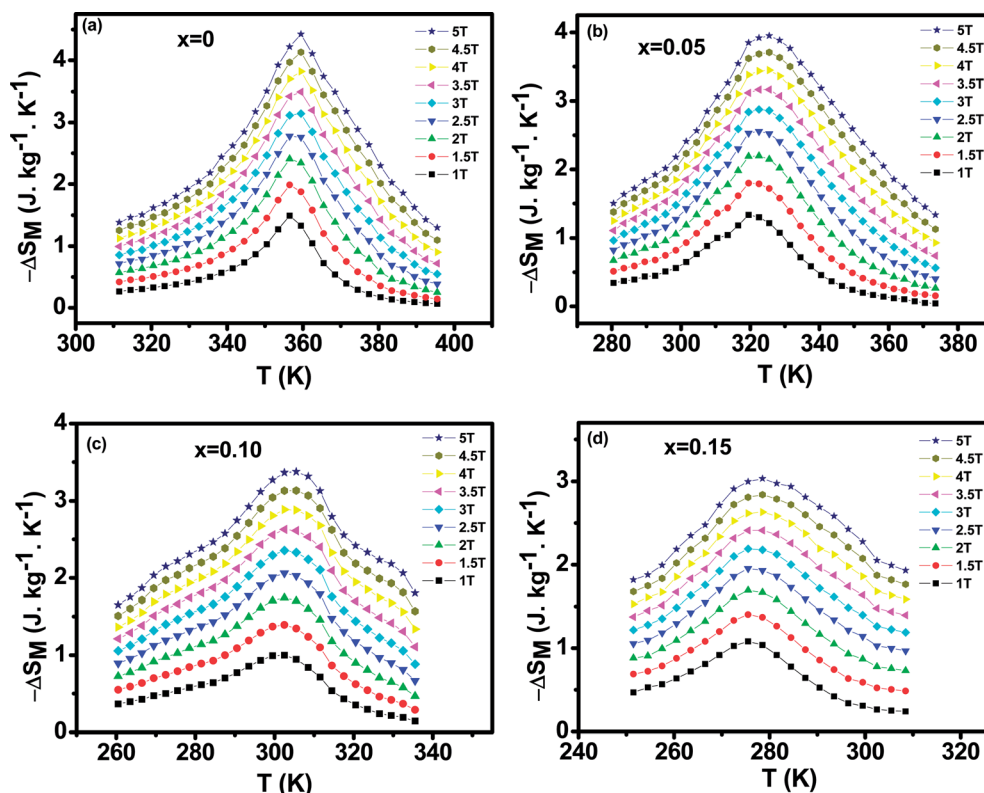


Fig. 7 The temperature dependence of the magnetic entropy change ($\Delta S_M$) under different applied magnetic fields (a) for $x = 0$, (b) for $x = 0.05$, (c) for $x = 0.10$ and (d) for $x = 0.15$.

**Table 3** Maximum entropy change $|\Delta S_M^{max}|$ and relative cooling power (RCP), for $La_{0.65}Ce_{0.05}Sr_{0.3}Mn_{1-x}Cu_xO_3$ ($0 \leq x \leq 0.15$), occurring at the Curie temperature ($T_C$) and under magnetic field variations, $\mu_0 H = 1$ T or $\mu_0 H = 5$ T, compared to several materials considered for magnetic refrigeration

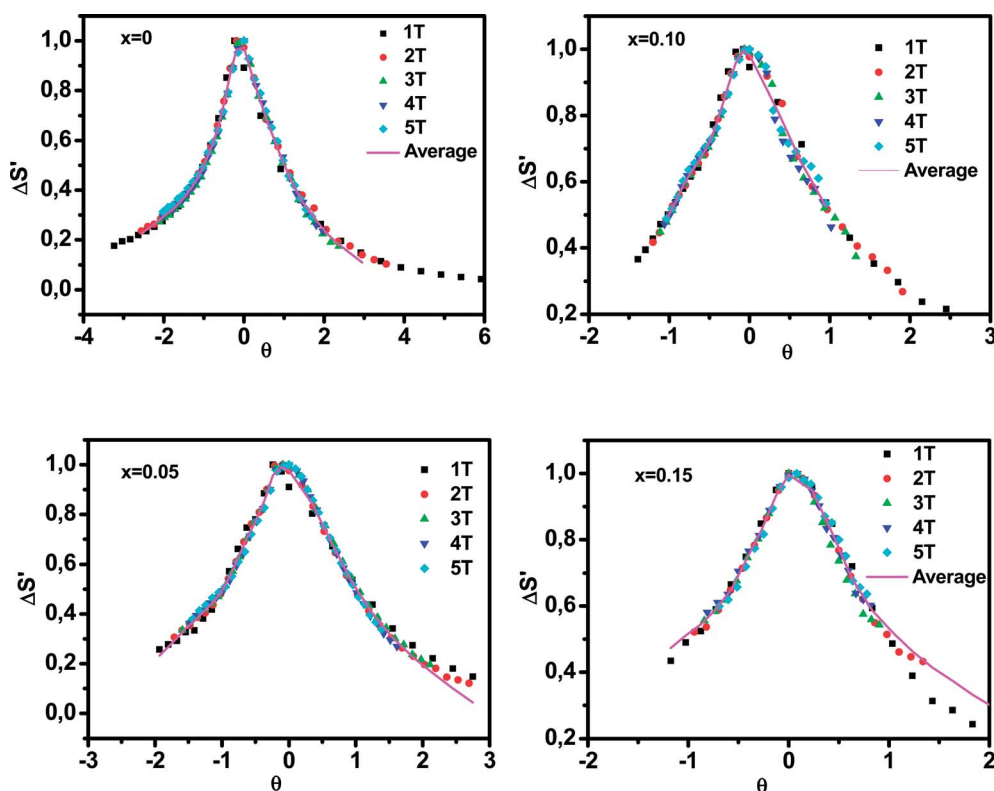| Composition | $T_C$ (K) | $\Delta H$ (T) | $\|-\Delta S_M^{max}$ (J kg$^{-1}$ K$^{-1}$)$\|$ | RCP (J kg$^{-1}$) | Ref. |
|---|---|---|---|---|---|
| Gd | 293 | 1 | 3.25 | — | 47 |
| $La_{0.77}Sr_{0.23}Mn_{0.9}Cu_{0.1}O_3$ | 325 | 1 | 4.41 | 57 | 26 |
| $La_{0.7}Sr_{0.3}Mn_{0.9}Cu_{0.1}O_3$ | 347 | 1 | 3.24 | — | 21 |
| $La_{0.65}Ce_{0.05}Sr_{0.3}MnO_3$ | 360 | 1 | 1.49 | 33 | This work |
| $La_{0.65}Ce_{0.05}Sr_{0.3}Mn_{0.95}Cu_{0.05}O_3$ | 330 | 1 | 1.34 | 44 | This work |
| $La_{0.65}Ce_{0.05}Sr_{0.3}Mn_{0.9}Cu_{0.1}O_3$ | 305 | 1 | 1.5 | 36 | This work |
| $La_{0.65}Ce_{0.05}Sr_{0.3}Mn_{0.85}Cu_{0.15}O_3$ | 275 | 1 | 1.08 | 28 | This work |
| $La_{0.67}Ba_{0.33}Mn_{0.98}Ti_{0.02}O_3$ | 310 | 1 | 0.93 | 45 | 17 |
| Gd | 293 | 5 | 9.5 | 410 | 48 |
| $La_{0.65}Ce_{0.05}Sr_{0.3}MnO_3$ | 360 | 5 | 4.43 | 132 | This work |
| $La_{0.65}Ce_{0.05}Sr_{0.3}Mn_{0.95}Cu_{0.05}O_3$ | 330 | 5 | 3.95 | 175 | This work |
| $La_{0.65}Ce_{0.05}Sr_{0.3}Mn_{0.9}Cu_{0.1}O_3$ | 305 | 5 | 3.37 | 102 | This work |
| $La_{0.65}Ce_{0.05}Sr_{0.3}Mn_{0.85}Cu_{0.15}O_3$ | 275 | 5 | 3.06 | 88 | This work |
| $La_{0.65}Eu_{0.05}Sr_{0.3}Mn_{0.9}Cr_{0.1}O_3$ | 310 | 5 | 3.35 | 207 | 16 |
| $La_{0.67}Ba_{0.33}Mn_{0.98}Ti_{0.02}O_3$ | 310 | 5 | 3.19 | 307 | 17 |

phenomenological universal curve, an analogous procedure to that described in ref. 51 has been used. It consists in normalizing the $\Delta S_M$ curves with respect to their maximum and rescaling the temperature axis as

$$\theta = -(T - T_C)/(T_{R1} - T_C) \quad \text{for } T \leq T_C,$$
$$\theta = -(T - T_C)/(T_{R2} - T_C) \quad \text{for } T \leq T_C, \quad (4)$$

where $T_{R1}$ and $T_{R2}$ are the two reference temperatures corresponding to the half maximum of $\Delta S_M(T_{R1}) = \Delta S_M(T_{R2}) =$ $\Delta S_M^{max}/2$. For the materials undergoing second order magnetic phase transition, the rescaled magnetic entropy change curves should follow a universal behavior. While the scaled $\Delta S_M$ curves do not collapse as a single curve, the materials undergo a first-order phase transition.[42]

Fig. 8 shows the universal curves constructed for the experimental $\Delta S_M$ ($T$, $H$) curves as a function of the rescaled temperature for $La_{0.65}Ce_{0.05}Sr_{0.3}Mn_{1-x}Cu_xO_3$ ($x = 0$, 0.10 and 0.15) samples. It can be clearly seen from this figure that all



**Fig. 8** Normalized $\Delta S_M$ versus rescaled temperature $\theta$ for $La_{0.65}Ce_{0.05}Sr_{0.3}Mn_{1-x}Cu_xO_3$, the solid line is the average curve.

normalized entropy change curves collapse into a single universal curve, which confirms that the PM–FM phase transition observed for our compounds is of a second-order. Hence, this result is consistent with the trends observed in the Arrott plots (Fig. 6).

The solid line corresponds to the average of the universal scaling. This average curve, once the temperature axis is back transformed from the reduced temperature to the unnormalized one, allows making extrapolations to lower temperatures for the high field data and obtaining a finer description of the peak for the low field curves.[52,53]

## 4.   Conclusion

In summary, we have studied the effect of copper doping lanthanum manganite ions on structural, magnetic and magnetocaloric properties of $La_{0.65}Ce_{0.05}Sr_{0.3}Mn_{1-x}Cu_xO_3$ ($0 \leq x \leq 0.15$) prepared using the Pechini sol–gel method. Rietveld refinement of XRD patterns shows that all samples crystallized in a rhombohedral structure with $R\bar{3}c$ space group. The Cu-doping induces the suppression of the one-electron bandwidth $W$ of $e_g$ electron due the variations of the bond length and bond angle, leading to destruction of the DE interaction. The Curie temperature and the maximum magnetic entropy change decrease with the increase in the Cu content. This is attributed to the structural distortion of $MnO_6$ octahedron and the changes in the valence states of the Cu and Mn ions upon Cu doping, weakening the ferromagnetic exchange interaction. A uniform phenomenological function that describes the magnetic entropy change is found for these materials, which provides good handle on designing of magnetocaloric materials for micro magnetic refrigerators.

The $La_{0.65}Ce_{0.05}Sr_{0.3}Mn_{0.95}Cu_{0.05}O_3$ sample is found to have a comparable MCE around 330 K with a maximum $\Delta S_M$ of 1.34 J kg$^{-1}$ K$^{-1}$ and a RCP of 44 J kg$^{-1}$ under a magnetic field change of 1 T, and can be considered as competitive candidate for magnetic refrigerant materials operating near room temperature.

## Conflicts of interest

There are no conflicts to declare.

## References

1 A. P. Ramirez, *J. Phys.: Condens. Matter*, 1997, **9**, 8171.

2 Z. B. Guo, Y. W. Du, J. S. Zhu, H. Huang, W. P. Ding and D. Feng, *Phys. Rev. Lett.*, 1997, **78**, 1142.

3 M. B. Salamon and M. Jaime, *Rev. Mod. Phys.*, 2001, **73**, 583.

4 E. Dagotto, T. Hotta and A. Moreo, *Phys. Rep.*, 2001, **344**, 1.

5 C. Zener, *Phys. Rev. B: Condens. Matter Mater. Phys.*, 1951, **82**, 403.

6 A. J. Millis, *Phys. Rev. B: Condens. Matter Mater. Phys.*, 1996, **53**, 8434.

7 M. Saleem and D. Varshney, *RSC Adv.*, 2018, **8**, 1600.

8 M. Oumezzine, S. Kallel, O. Peña, N. Kallel, T. Guizouarn, F. Gouttefangeas and M. Oumezzine, *J. Alloys Compd.*, 2014, **582**, 640.

9 A. Coskun, E. Tasarkuyu, A. E. Irmak, M. Acet, Y. Samancıoglu and S. Akturk, *J. Alloys Compd.*, 2015, **622**, 796.

10 S. Zhao, X.-J. Yue and X. Liu, *Ceram. Int.*, 2017, **43**, 13240.

11 A. E.-M. A. Mohamed and B. Hernando, *Phys. Lett. A*, 2016, **380**, 1763.

12 R. Thaljaoui, M. Pękała, J. F. Fagnard and P. Vanderbemden, *J. of Rare Earths*, 2017, **35**, 875.

13 S. Vadnala and S. Asthana, *J. Magn. Magn. Mater.*, 2018, **446**, 68.

14 M. S. Anwar, F. Ahmed and B. Heun Koo, *Ceram. Int.*, 2015, **41**, 5821.

15 M. Zarifi, P. Kameli, M. Mansouri, H. Ahmadv and H. Salamati, *Solid State Commun.*, 2017, **262**, 20.

16 R. Bellouz, M. Oumezzine, E. K. Hlil and E. Dhahri, *J. Magn. Magn. Mater.*, 2015, **375**, 136.

17 M. Oumezzine, O. Peña, S. Kallel and M. Oumezzine, *J. Alloys Compd.*, 2012, **539**, 116.

18 I. Betancourt, L. Lopez Maldonado and J. T. Elizalde Galindo, *J. Magn. Magn. Mater.*, 2016, **401**, 812.

19 J. C. Debnath and J. Wang, *Phys. B*, 2017, **504**, 58.

20 P. T. Phong, L. V. Bau, L. C. Hoan, D. H. Manh, N. X. Phuc and I.-J. Lee, *J. Alloys Compd.*, 2016, **656**, 920.

21 M. H. Phan, H. X. Peng, S. C. Yu, N. D. Tho and N. Chau, *J. Magn. Magn. Mater.*, 2005, **285**, 199.

22 M. S. Anwar, S. Kumar, F. Ahmed, S. Nae Heo, G. W. Kim and B. Heun Koo, *J. Electroceram.*, 2013, **30**, 46.

23 Q. T. Phung, V. K. Vu, A. B. Ngac, H. S. Nguyen and N. N. Hoang, *J. Magn. Magn. Mater.*, 2012, **324**, 2363.

24 C. Shang, Z. C. Xia, M. Wei, Z. Jin, B. R. Chen, L. R. Shi, Z. W. Ouyang, S. Huang and G. L. Xiao, *J. Magn. Magn. Mater.*, 2016, **416**, 357.

25 M. El-Hagary, Y. A. Shoker, S. Mohammad, A. M. Moustafa, A. Abd El-Aal, H. Michor, M. Reissner, G. Hilscher and A. A. Ramadan, *J. Alloys Compd.*, 2009, **47**, 468.

26 P. Thamilmaran, M. Arunachalam, S. Sankarrajan, K. Sakthipandi, E. James Jebaseelan Samuel and M. Sivabharathy, *J. Magn. Magn. Mater.*, 2017, **443**, 29.

27 K. Y. Wang, W. H. Song, J. M. Dai, S. L. Ye, S. G. Wang, J. Fang, J. L. Chen, B. J. Gao, J. J. Du and Y. P. Sun, *J. Appl. Phys.*, 2001, **90**, 6263.

28 T. L. Phan, P. Q. Thanh, N. H. Sinh, Y. D. Zhang and S. C. Yu, *IEEE Trans. Magn.*, 2012, **48**, 1293.

29 K. Yadav, M. P. Singh, F. S. Razavi and G. D. Varma, *Mater. Chem. Phys.*, 2012, **137**, 323.

30 M. S. Kim, J. B. Yang, J. Medvedeva, W. B. Yelon, P. E. Parris, W. J. James and J. Phys, *Condens. Matter*, 2008, **20**, 255228.

31 M. S. Kim, J. B. Yang, P. E. Parris, Q. Cai, X. D. Zhou, W. J. James, W. B. Yelon, D. Buddhikot and S. K. Malik, *J. Appl. Phys.*, 2005, **97**, 714.

32 T. Roisnel and J. Rodriguez-Carvajal, *Computer Program FULLPROF*, LLBLCSIM, May 2003.

33 R. D. Shannon, *Acta Crystallogr., Sect. A: Cryst. Phys., Diffr., Theor. Gen. Crystallogr.*, 1976, **32**, 751.

34 K. Momma and F. Izumi, *J. Appl. Crystallogr.*, 2011, **44**, 1272.

35 R. Bellouz, M. Oumezzine, A. Dinia, G. Schmerber, E. Hlil and M. Oumezzine, *RSC Adv.*, 2015, **5**, 64557.

36 L. M. Carrón, A. de Andrés, M. J. Martínez-Lope, M. T. Casais and J. A. Alonso, *Phys. Rev. B: Condens. Matter Mater. Phys.*, 2002, **66**, 174303.

37 N. Van Minh and I.-S. Yang, *Vib. Spectrosc.*, 2006, **42**, 353.

38 M. Oumezzine, O. Hassayoun, R. Bellouz, H. B. Sales and E. K. Hlil, *J. Alloys Compd.*, 2017, **729**, 156.

39 D. Varshney and M. W. Shaikh, *J. Alloys Compd.*, 2014, **589**, 558.

40 G. De Marzi, H. J. Trodahl, J. Bok, A. Cantarero and F. Sapina, *Solid State Commun.*, 2003, **127**, 259.

41 B. Martinez, V. Laukhin, J. Fontcuberta, L. Pinsard and A. Revcolevschi, *Phys. Rev. B: Condens. Matter Mater. Phys.*, 2002, **66**, 054436.

42 J. J. Blanco, M. Insausti, I. Gil de Muro, L. Lezama and T. Rojo, *J. Solid State Chem.*, 2006, **179**, 623.

43 L. M. R. Martinez and J. P. Attfield, *Phys. Rev. B: Condens. Matter Mater. Phys.*, 1996, **54**, 5622.

44 B. K. Banerjee, *Phys. Lett.*, 1964, **12**, 16.

45 J. S. Amaral and V. S. Amaral, *J. Magn. Magn. Mater.*, 2010, **322**, 1552.

46 N. A. De Oliveira and P. J. Von Ranke, *Phys. Rev. B: Condens. Matter Mater. Phys.*, 2008, **77**, 214439.

47 M. Földeàki, R. Chahine and T. K. Bose, *J. Appl. Phys.*, 1995, **77**, 3528.

48 K. A. Gschneidner Jr, V. K. Pecharsky and A. O. Tsokol, *Rep. Prog. Phys.*, 2005, **68**, 1479.

49 V. Franco and A. Conde, *Int. J. Refrig.*, 2010, **33**, 465.

50 V. Franco, R. Caballero-Flores, A. Conde, Q. Y. Dong and H. W. Zhang, *J. Magn. Magn. Mater.*, 2009, **321**, 1115.

51 V. Franco, A. Conde, J. M. Romero-Enrique and J. S. Blázquez, *J. Phys.: Condens. Matter*, 2008, **20**, 285207.

52 L. Zhang, J. Fan, W. Tong, L. Ling, L. Pi and Y. Zhang, *Phys. B*, 2012, **407**, 3543.

53 V. M. Pridaa, V. Franco, V. Vega, J. L. Sanchez-Llamazares, J. J. Sunol, A. Conde and B. Hernand, *J. Alloys Compd.*, 2011, **509**, 190.